World Electric Vehicle Journal

Article

Distributed Intelligent Vehicle Path Tracking and Stability Cooperative Control

Zhaoxue Deng *, Yangrui Zhang and Shuen Zhao

School of Electrical and Mechanical Engineering and Vehicle Engineering, Chongqing Jiaotong University, Chongqing 400074, China; zyrdlcx@163.com (Y.Z.); zse0916@163.com (S.Z.)
* Correspondence: dengzhaoxue@126.com

Abstract: To enhance the path tracking capability and driving stability of intelligent vehicles, a controller is designed that synergizes active front wheel steering (AFS) and direct yaw moment (DYC), specifically tailored for distributed-drive electric vehicles. To address the challenge of determining the weight matrix in the linear quadratic regulator (LQR) algorithm during the path tracking design for intelligent vehicles on conventional roads, a genetic algorithm (GA)-optimized LQR path tracking controller is introduced. The 2-degree-of-freedom vehicle dynamics error model and the desired path information are established. The genetic algorithm optimization strategy, utilizing the vehicle's lateral error, heading error, and output front wheel steering angle as the objective functions, is employed to optimally determine the weight matrices Q and R. Subsequently, the optimal front wheel steering angle control (AFS) output of the vehicle is calculated. Under extreme operating conditions, to enhance vehicle dynamics stability, while ensuring effective path tracking, the active yaw moment is crafted using the sliding mode control with a hyperbolic tangent convergence law function. The control weights of the sliding mode surface related to the center-of-mass lateral declination are adjusted based on the theory of the center-of-mass lateral declination phase diagram, and the vehicle's target yaw moment is calculated. Validation is conducted through Matlab/Simulink and Carsim co-simulation. The results demonstrate that the genetic algorithm-optimized LQR path tracking controller enhances vehicle tracking accuracy and exhibits improved robustness under conventional road conditions. In extreme working conditions, the designed path tracking and stability cooperative controller (AFS+DYC) is implemented to enhance the vehicle's path tracking effect, while ensuring its driving stability.

Keywords: intelligent vehicles; genetic algorithm; path tracking; direct yaw moment; cooperative control

Citation: Deng, Z.; Zhang, Y.; Zhao, S. Distributed Intelligent Vehicle Path Tracking and Stability Cooperative Control. *World Electr. Veh. J.* **2024**, *15*, 89. https://doi.org/10.3390/wevj15030089

Academic Editor: Grzegorz Sierpiński

Received: 31 December 2023
Revised: 16 January 2024
Accepted: 23 February 2024
Published: 28 February 2024

1. Introduction

The continuous advancement of smart car technology presents solutions to ongoing challenges such as traffic congestion, energy limitations, and traffic safety [1]. The integration of environment sensing, decision-making, planning, and motion control in intelligent driving vehicles has been a prominent research focus in recent years within the automotive field [2]. Among these components, vehicle motion control poses a critical challenge in achieving intelligent driving, encompassing both lateral path tracking control and longitudinal vehicle control. Under normal operating conditions, the aforementioned controllers demonstrate effective path tracking. However, under extreme conditions such as high speed and low adhesion roads, the vehicle is prone to slipping and instability, posing a safety concern for vehicle operation. This paper explores a distributed intelligent vehicle equipped with four-wheel independent drive motors, serving as a platform for stability systems like direct yaw torque control. It synergistically integrates with the DYC controller based on the path tracking front wheel steering control (AFS) to enhance the safety and stability of the vehicle. Hence, there is significant research value in synthesizing path tracking accuracy and synergistic control of vehicle stability for distributed-drive electric vehicles [3].

Path tracking control involves tracking the desired path in the lateral direction of the vehicle, requiring attributes such as good timeliness and robustness. Commonly used vehicle path tracking methods include PID control [4], sliding mode control [5], fuzzy control [6], model predictive control [7], and linear quadratic optimal control [8]. PID control is extensively employed in engineering; however, parameter determination is a time-intensive process. Model predictive control demands the establishment of a precise system model, incorporating calculations that consider vehicle dynamics constraints. While it offers better control accuracy, the increased calculation time diminishes real-time performance [9]. Gao L [10] designed a lateral motion controller for an intelligent vehicle using linear-quadratic optimal control (LQR) theory and designed a feed-forward controller to eliminate the lateral error of the vehicle, but did not accurately describe the controller parameter settings. Based on the vehicle error dynamics model, the path tracking controller is designed. The genetic algorithm (GA) is used to optimize the controller parameters to improve the vehicle's path tracking ability. The optimization algorithm and linear quadratic controller were combined to design the path tracking controller for the vehicle in this paper. Vehicle active steering exhibits robust operational stability in regular working conditions. However, under extreme working conditions, the lateral force of tires gradually reaches saturation as the wheel angle increases, leading to vehicle instability. Research scholars Zhang L [11] and Nie Y [12] proposed that, based on active steering, the lack of lateral tire force is compensated by the longitudinal force of the wheels, thereby enhancing vehicle stability under extreme operating conditions. Chen T [13] designed a sliding mode controller that considers both path tracking and stability control. They proposed a tire force optimization allocation scheme to achieve desired path tracking on good road surfaces but did not investigate stability control on icy road surfaces. Zhao S [14] suggested the coordinated control of active front wheel steering and DYC to harmonize the functions of active steering and electric stability control. Utilizing vehicle phase plane theory facilitates seamless switching between controllers, improving the driving state and stability of the vehicle. Liang Y [15] addressed the challenge of potential destabilization in high-speed, lateral vehicle control by proposing an integrated control system of active steering and DYC. This system is based on driver operation characteristics and vehicle phase plane theory. Under conditions involving a large turning angle and high-speed obstacle avoidance, stable vehicle control is achieved, albeit at a reasonable sacrifice of the operational stability performance, to enhance overall driving performance.

Taking the distributed intelligent vehicle as the research object, this paper designs the LQR path tracking controller, optimized based on a genetic algorithm for vehicle lateral path tracking. Additionally, pre-scanning control is introduced to enhance the vehicle's path tracking effectiveness. To ensure the vehicle's path tracking ability and to simultaneously enhance vehicle stability, this paper designs an active traverse moment controller. The sliding mode controller, based on a hyperbolic tangent function, is employed to track the desired traverse angular velocity. Concurrently, the control weights of the sliding mode surface of the vehicle's sideslip angle are adjusted based on the theory of the vehicle's sideslip angle phase diagram, aiming to achieve a balance between path tracking accuracy and dynamic stability. Ultimately, the effectiveness of the designed controller is verified through a comprehensive simulation involving Matlab/Simulink and Carsim.

2. Vehicle Path Error Model

The establishment of a reference model of vehicle motion is the basis for the determination of the path tracking controller, based on a physical system to establish the vehicle two-degree-of-freedom dynamics and vehicle tracking error dynamics models.

2.1. Two-Degree-of-Freedom Vehicle Model

In order to enhance the accuracy of vehicle path tracking and streamline the vehicle model, a single-track, linear 2-degree-of-freedom vehicle model, encompassing lateral and transverse motions, was established, as depicted in Figure 1. The rear wheels of the vehicle model do not undergo steering, and the impact of suspension effects on the vehicle is disregarded.

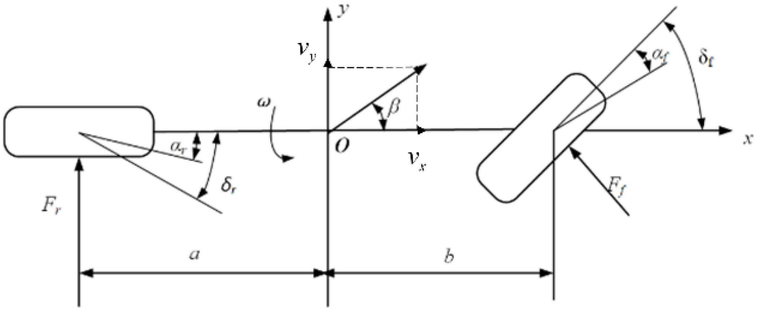

Figure 1. Monorail vehicle dynamics model.

The differential equations of motion for the vehicle are derived from Newton's second law:

$$\begin{cases} \dot{v}_y = \frac{K_f+K_r}{mv_x}v_y + (\frac{aK_f-bK_r}{mv_x} - v_x)\omega_r - \frac{K_f}{m}\delta_f \\ \dot{\omega}_r = \frac{aK_f-bK_r}{I_z}v_y + \frac{a^2K_f+b^2K_r}{I_zv_x}\omega_r - \frac{aK_f}{I_z}\delta_f \end{cases} \tag{1}$$

In the formula: v_x and v_y are the longitudinal and lateral velocities of the vehicle, respectively; ω_r is the transverse angular velocity of the vehicle; δ_f is the front wheel angle of the vehicle; I_z is the moment of inertia of the vehicle; $I_z = 1536.7\ (kN \cdot m^2)$; a, b is the distance from the center of mass of the vehicle to the front and rear axes, $a = 1.015$ m, $b = 1.895$ m; vehicle mass is $m = 1412$ kg; vehicle front wheel side deflection stiffness is $K_f = -145,000$ (kN·rad^{-1}); and vehicle rear wheel side deflection stiffness is $K_r = -84,400$ (kN·rad^{-1}).

2.2. Vehicle Path Tracking Error Dynamics Modeling

In the control of vehicle path tracking, the tracking error model stands out as a frequently employed vehicle motion model. By projecting the vehicle's coordinate points from geodetic coordinates to the natural coordinate system, an error dynamics model is established with the vehicle's lateral error and heading error as state variables [16], as illustrated in Figure 2, where the lateral distance deviation e_d refers to the shortest straight line distance from the vehicle center of mass position to the desired path. θ refers to the heading angle of the vehicle, and θ_r refers to the heading angle of the vehicle projection point H on the reference path. Considering the small lateral deviation of the center of mass of the vehicle, the heading angle of the vehicle θ is replaced by the vehicle traverse angle φ. Vehicle heading deviation means the difference between the actual vehicle yaw angle and the desired heading angle $e_\varphi = \varphi - \theta_r$.

The lateral error value of the vehicle is:

$$e_d = (y - yr)\cos\varphi - (x - xr)\sin\varphi \tag{2}$$

where x, y are the transverse and longitudinal coordinates of the vehicle; xr, yr are the transverse and longitudinal coordinates of the reference path; and φ is the actual traverse angle of the vehicle.

Assuming the vehicle is moving at a constant speed with a large turning radius R, the theoretical values for the rate of change of the vehicle's heading angle and its acceleration are:

$$\dot{\varphi} = \frac{v_x}{R}; \frac{{v_x}^2}{R} = v_x\dot{\theta}_r \tag{3}$$

where θ_r is the desired heading angle and R is the vehicle turning radius.

The heading error and lateral error rates are calculated as follows.

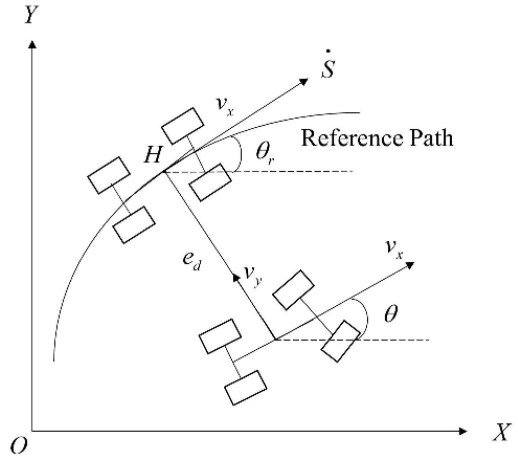

Figure 2. Error model of vehicle dynamics.

$$\begin{cases} e_\varphi = \varphi - \theta_r \\ \dot{e}_d = \dot{y} + v_x(\dot{\varphi} - \dot{\theta}_r) \end{cases} \tag{4}$$

Under the conventional road, the change of the vehicle's heading angular velocity is small, ignoring the effect of $\dot{\theta}_r$, substituting Equation (4) into Equation (1) to obtain $\ddot{e}_d$, $\ddot{e}_\varphi$, and writing e_{rr} in the form of state-space equations:

$$\dot{e}_{rr} = Ae_{rr} + Bu + C\dot{\theta}_r \tag{5}$$

Among them: $e_{rr} = \begin{pmatrix} e_d & \dot{e}_d & e_\varphi & \dot{e}_\varphi \end{pmatrix}^T$ and $u = \delta_f$

$$A = \begin{bmatrix} 0 & 1 & 0 & 0 \\ 0 & \frac{K_f+K_r}{mv_x} & -\frac{K_f+K_r}{m} & \frac{aK_f-bK_r}{mv_x} \\ 0 & 0 & 0 & 1 \\ 0 & \frac{aK_f-bK_r}{I_zv_x} & -\frac{aK_f-bK_r}{I_z} & \frac{a^2K_f+b^2K_r}{I_zv_x} \end{bmatrix}, B = \begin{bmatrix} 0 \\ \frac{-K_f}{m} \\ 0 \\ \frac{aK_f}{I_z} \end{bmatrix}, C = \begin{bmatrix} 0 \\ \frac{aK_f-bK_r}{mv_x} - v_x \\ 0 \\ \frac{a^2K_f+b^2K_r}{I_zv_x} \end{bmatrix}.$$

3. Vehicle Transverse Longitudinal Controller Design

The vehicle lateral and longitudinal controller frames are shown in Figure 3. In the context of lateral vehicle control, the active front wheel steering path tracking controller employs an optimization approach that integrates the linear quadratic (LQR) path tracking control algorithm and the genetic algorithm (GA) to determine the optimal parameters of the path tracking controller. Leveraging the vehicle lateral dynamics error model, the GA-LQR path tracking controller is formulated with the objective function serving as the optimization goal, aiming to enhance the path tracking capability of the individually front wheel steering (AFS) vehicle.

For the longitudinal control of the vehicle, a PID speed-tracking controller is employed to ensure adherence to the desired vehicle speed, generating the requisite drive torque for effective speed tracking. In the realm of vehicle stability control, the AFS-derived front wheel angle feeds into both the ideal vehicle model and the phase plane coordination layer to ascertain the vehicle stability domain value accurately. This coordination involves assigning a weight share for center-of-mass lateral deflection control within the direct transverse torque controller, facilitating the calculation of the target transverse torque for the distributed-drive vehicle. Subsequently, the lower-layer torque distribution controller tracks the driving force output from the upper layer controller, taking into consideration both the direct transverse moment and speed calculations. Additionally, considering the road adhesion coefficient condition, the optimization objective is to optimally distribute the four-wheel torque, with the minimum tire loading rate guiding this optimization. This optimized four-wheel torque is differentially distributed and ultimately conveyed from the motor model to the Carsim vehicle, forming a closed loop system.

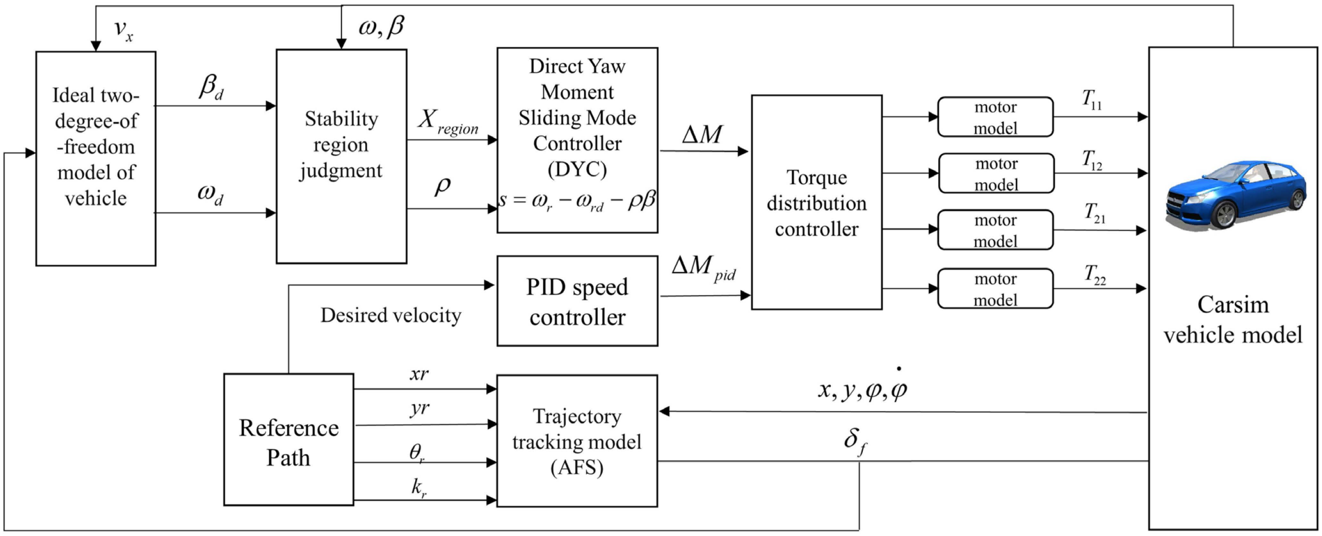

Figure 3. Vehicle transverse and longitudinal control flowchart.

3.1. Vehicle Longitudinal Controller

To ensure the consistent tracking of the upper desired speed by the vehicle, mitigating the impact of other control system effects, a longitudinal vehicle speed controller is crafted employing the PID control principle. The control rate of the PID vehicle speed controller is:

$$T_{pid} = K_p e_v(t) + K_i \int_0^t e_v(t) + K_d \frac{de_v(t)}{dt} \tag{6}$$

where e_v is the deviation value between the ideal speed and the actual speed and T_{pid} is the total wheel torque output from the speed controller. K_p, K_i, and K_d are the proportional, integral, and differential terms of the PID controller parameters, respectively.

The motor torque, T_{pid}, derived by the PID speed-tracking controller is distributed to the four motor models using an equal distribution:

$$T_{ij} = \frac{1}{4} T_{pid} \quad ij = 11, 12, 21, 22 \tag{7}$$

where T_{11}, T_{12}, T_{21}, T_{22} is the torque output value of the four motors.

The conventional powertrain of the Carsim vehicle undergoes substitution with a model of the motor system, wherein the motor is responsible for supplying the wheel drive torque. When concentrating exclusively on the interplay between the targeted torque and the actual torque derived from the motor, the motor model can be streamlined into a second-order transfer function, offering a representation of its dynamic torque output response. This torque transfer function is articulated as follows:

$$G(s) = \frac{T_d}{T_d^*} = \frac{1}{2\zeta^2 s^2 + 2\zeta s + 1} \tag{8}$$

where T_d^* is the target torque obtained by the controller, T_d is the output torque of the hub motor, and ζ is the motor system time constant, which can usually be obtained empirically. s is the transfer function value.

3.2. Design of Vehicle Lateral Controller

Linear quadratic optimal control theory (LQR) is widely used in models where the controlled object is a state space. Path tracking controllers are designed based on the vehicle error dynamics model, and the control system performance metrics J for:

$$J = \frac{1}{2}\int_0^\infty [{e_{rr}}^T(t)Qe_{rr}(t) + u^T Ru]dt \tag{9}$$

where Q is the vehicle error weight matrix and R is the control quantity weight matrix.

In order to find the minimum value of the performance index function J, the variational method is utilized to solve the quadratic optimization problem, constructing the quadratic form in the general form of:

$$H = -\frac{1}{2}[{e_{rr}}^T(t)Qe_{rr}(t) + u^T(t)Ru(t)] + \lambda^T[Ae_{rr}(t) + Bu(t)] \tag{10}$$

The Hamiltonian function is derived from H, and the optimal control signal of the controller is solved at its value 0:

$$u^*(t) = R^{-1}B^T\lambda(t) = R^{-1}B^T P(t)e_{rr}(t) \tag{11}$$

where $P(t)$ is obtained by solving the following Riccati equation:

$$PA + A^T P - PBR^{-1}BP^T + Q = 0 \tag{12}$$

The optimal control rate feedback matrix of the LQR controller is $K = R^{-1}B^T P$, and the computed optimal front wheel angle control law is:

$$\delta_f(k) = -Ke_{rr}(k) \tag{13}$$

where $K = [K_1, K_2, K_3, K_4]$, A, B values are only related to the vehicle parameters.

3.3. Design of Pre-Sighting Points for Path Tracking Control

Intelligent vehicles exhibit superior path tracking effects at low speeds. However, at higher speeds, vehicle stability diminishes due to the limited vehicle control time. In this study, pre-aiming time is introduced in addition to path tracking control. This enables the vehicle to make advanced predictions regarding path changes, thereby mitigating the large front wheel angle calculations and jitter phenomena associated with the limited control time. The pre-scan time is not a fixed value; rather, it needs to be increased proportionally as the speed of the vehicle increases. The trajectory of the vehicle after the specified time is illustrated in Figure 4.

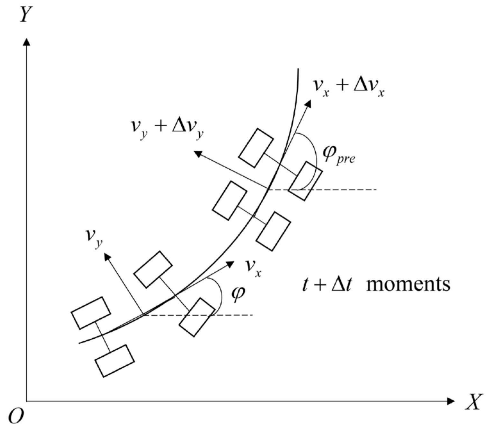

Figure 4. Pre-aiming for vehicle path tracking.

The pre- aiming control incorporates the predicted path information into discrete path points for subsequent update calculations. The computed path information is represented by the following equation:

$$\begin{cases} x_{pre} = x + v_x \Delta t \cos\varphi - v_y \Delta t \sin\varphi \\ y_{pre} = y + v_y \Delta t \cos\varphi + v_x \Delta t \sin\varphi \\ \varphi_{pre} = \varphi + \dot{\varphi} \Delta t \\ \dot{\varphi}_{pre} = \dot{\varphi} \end{cases} \tag{14}$$

where x_{pre} and y_{pre} represent the horizontal and vertical coordinates of the pre-sighting point, φ_{pre} is the transverse angle of the pre-sighting point, and Δt is the pre-sighting time.

3.4. Genetic Optimization Algorithm

The efficacy of the LQR path tracking controller is intricately linked to the Q,R weighting matrix, where an elevated Q value enhances vehicle path tracking accuracy, and a heightened R value mitigates control loss. Traditionally, these two weighting matrix values undergo manual adjustments and trials, a time-consuming process lacking theoretical support. This paper addresses this challenge by employing a genetic optimization algorithm to ascertain the optimal controller weighting matrix value for achieving the most effective path tracking. The genetic algorithm [17] replicates the evolutionary processes observed in nature. The optimization process encompasses initialization, coding, fitness function calculation, selection, crossover, mutation, and termination condition assessment, ultimately producing results aligned with the optimization goal, as depicted in Figure 5.

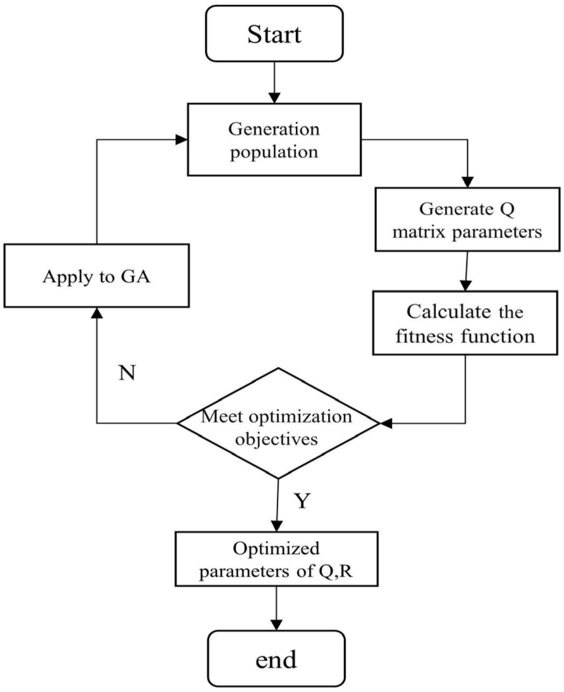

Figure 5. Flowchart of the genetic algorithm.

The genetic algorithm randomly generates the initial population under specified constraints. Each individual in the population is assigned values for the coefficients q1~q5 of the Q and R matrices. The controller computes the optimal feedback gain matrix and the front wheel angle of the vehicle, then it executes the path tracking model to obtain the fitness value. The algorithm terminates when the fitness value satisfies the specified termination condition. Otherwise, genetic manipulation continues to generate a new population generation, and the process repeats until convergence. The algorithm iteratively solves for the optimal Q and R values. The genetic algorithm parameters are configured with a population size of 100, a maximum number of iterations set to 15, 10 individuals per generation, a crossover probability of 0.4, and individual values within the range of 1–100. The fitness function of the genetic algorithm is crafted to minimize lateral and heading errors while keeping control energy consumption relatively low. Consequently, the performance index function comprises three terms, and the fitness function J [18] is formulated as:

$$J = \omega_1 \Delta e_d + \omega_2 \Delta e_\varphi + \omega_3 \Delta \delta_f \tag{15}$$

where $\omega_1, \omega_2, \omega_3$ are the weight coefficients of the occupancy fitness functions of Δe_d, Δe_φ, $\Delta\delta_f$, where a larger weight coefficient indicates a higher control importance and is the unit of uniform variable, and Δe_d, Δe_φ, $\Delta\delta_f$ are the root mean square values of lateral error, heading error, and the front wheel turning angle of the vehicle, respectively.

4. Direct Yaw Torque Controller

A four-wheel drive electric vehicle can generate an active transverse moment using the drive/brake torque difference between the left and right sided wheels, which can be used for vehicle stability enhancement based on path tracking for intelligent vehicles. In order to avoid the risk of the destabilization of the vehicle under extreme operating conditions, the center of mass lateral deflection angle is introduced in the sliding mode surface. By fitting the vehicle tire side deflection force, the phase diagram of the center of mass side deflection angle is drawn based on the phase plane theory, and the instability of the vehicle in different working conditions is calculated. Based on the hyperbolic tangent function of the sliding mode control design of the active transverse moment, the control weights of the center of mass side deflection angle in the sliding mode surface of the active transverse moment are adjusted by the degree of instability of the vehicle, to ensure that the vehicle path tracking and stability have a better control effect.

4.1. Vehicle Stability Judgment

The nonlinear characteristics of a vehicle are primarily influenced by its tires. At small tire lateral deflection angles, the lateral deflection force is linear. As the tire lateral deflection angle increases, the upward trend of the lateral deflection force gradually slows down. During this phase, the lateral deflection stiffness value of the tire experiences a steep decrease.

Tires primarily operate in the nonlinear region during the driving process. To model the nonlinear tire data [19] the lateral force data for a 215/R17 tire are fitted using the Magic Tire formula:

$$F_y = D_y \sin\left\{C_y \arctan\left[B_y a - E_y\left(B_y a - \arctan(B_y a)\right)\right]\right\} \tag{16}$$

where considering the road surface μ adhesion coefficient on the tire model parameters, $D_y = \mu F_z$; $C_y = (5/4 - \mu/4)C_y$; $B_y = (2-\mu)B_y$; D_y is the peak factor; C_y is the shape factor; B_y is the stiffness factor; and E_y is the curvature factor. Where F_{zr} is the front and rear wheel vertical loads in the road conditions $\mu = 1$, the tire lateral force under different vertical loads for data fitting. The fitting results are shown in Figure 6, where $B_y = 5.263$; $C_y = 2.839$; and $E_y = 1.228$.

The phase plane method is used to determine the stability of the vehicle under different state parameters. Because the $\beta - \omega_r$ phase plane is affected by wheel angle and speed, it is difficult to judge the stability domain of the vehicle. This paper adopts the method of the $\beta - \dot{\beta}$ phase plane, which can accurately judge both the stable and unstable working conditions of the vehicle. Based on Equation (1) to establish the whole vehicle model equation, the second-order autonomous system of the vehicle is as follows:

$$\begin{cases} \dot{\beta} = f_1(\beta, w_r) \\ \dot{\omega_r} = f_2(\beta, w_r) \end{cases} \tag{17}$$

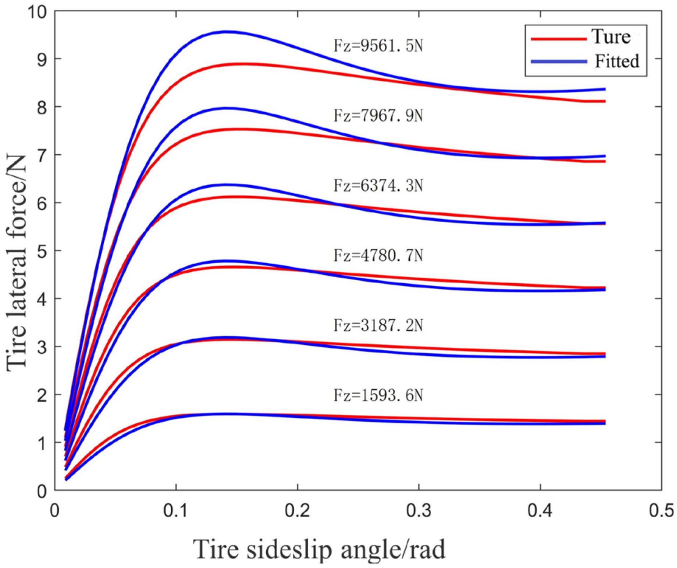

Figure 6. Fitting of tire cornering force.

Setting the vehicle speed at 120 km/h, the road surface adhesion coefficient at 0.7, and the front wheel turning angle at 0°, the different initial values of $(\beta(0), \omega_r(0))$ are set in a certain range for Equation (16), and, according to the theory of the phase plane, the $\beta - \dot{\beta}$ phase plane diagram of the vehicle is plotted as shown in Figure 7.

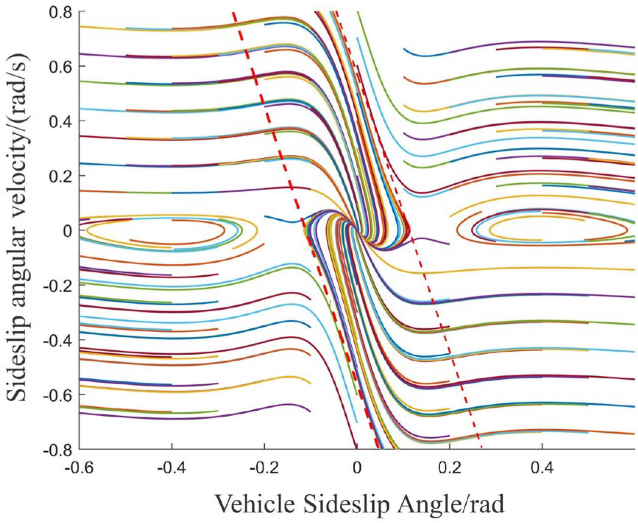

Figure 7. Mass center side slip angle phase plane.

On the phase plane image of the vehicle's center of mass side deviation angle, the double straight line method is used to divide the stable boundary of the vehicle, two symmetrical straight lines divide the vehicle into stable and unstable regions, and, through $\beta - \dot{\beta}$, the phase diagram is able to judge the vehicle's steady state in different road attachment coefficients and speeds, and the expression for the stable region in which the vehicle is located is:

$$\left|\dot{\beta} + B_1\beta\right| \leq B_2 \tag{18}$$

where B_1 is the slope of the boundary line, B_2 is the intercept of the boundary line and B_1 and B_2 are affected by the phase plane.

After plotting the phase diagram of the vehicle center of mass lateral deflection angle at different speeds and different road surface attachment coefficients, some of the data are shown in Table 1 below.

Table 1. Stable boundaries of the phase plane under different working conditions.

V_X(km/h)	μ	B_1	B_2
60	0.2	3.96	0.39
60	0.4	−6.10	0.70
60	0.6	6.71	0.75
90	0.4	4.76	0.55
90	0.6	5.93	0.70
90	0.8	6.76	0.84
120	0.6	5.60	0.62
120	0.8	6.17	0.70
120	1.0	7.51	0.94

From the data in Table 1, it can be seen that the curvature and intercept of the stabilizing boundary of the vehicle gradually increase with the increase in the road surface attachment coefficient. When the road surface attachment coefficient is small, the stabilization region of the vehicle is small and prone to instability. Different vehicle speeds are also added to the considered range and the obtained stability boundary range is plotted as shown in Figure 8.

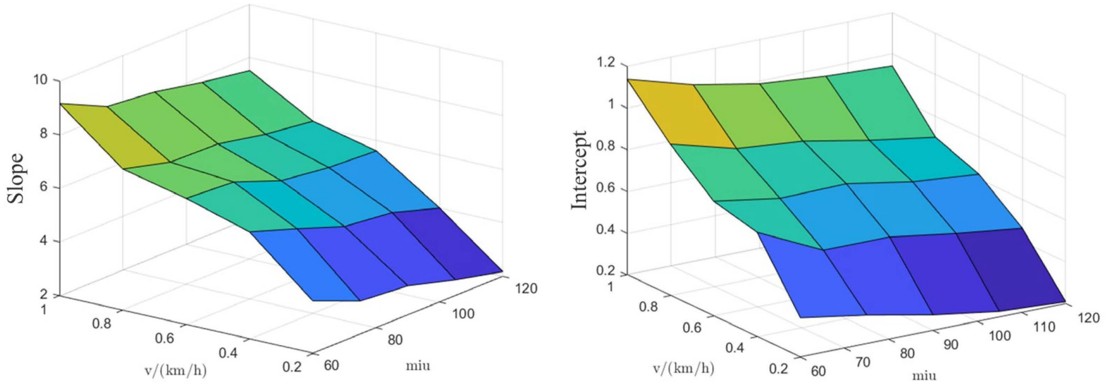

Figure 8. Effect of speed and pavement attachment coefficient on intercept and slope.

Taking the data from Table 1 and fitting the data by a polynomial, the boundary equations of the phase plane stability domain for a vehicle speed of 120km/h with a pavement attachment coefficient of $u = 0.3$ are obtained as:

$$\begin{cases} B_1 = -3.555\mu^2 + 10.69\mu + 0.247 \\ B_2 = -0.178\mu^2 + 1.07\mu + 0.024 \end{cases} \tag{19}$$

When the state point $(\beta, \dot{\beta})$ of the vehicle satisfies $\left|\dot{\beta} + B_1\beta\right| \leq B_2$, the vehicle is in the stable region; however, when it does not satisfy this, the vehicle is in the region of instability at this time. The distance from the state point to the boundary of the stabilized region is called the degree of destabilization ρ, and the formula for calculating the degree of destabilization of the phase plane is as follows:

$$\rho = \left|\frac{1}{B_2}\dot{\beta} + \beta\frac{B_1}{B_2}\right| \tag{20}$$

4.2. Direct Yaw Torque Controller

The direct traverse moment control has a more obvious effect on the control of the vehicle’s traverse angular velocity, and also has some effect on the center of mass side deflection angle. The sliding mode variable structure control system is used to design the target yaw moment control system; the vehicle parameter uptake and the external disturbance of the vehicle have less influence on the controller, and the control system has good robustness. In order to balance the relationship between path tracking and stability, both the vehicle’s center of mass lateral deflection angle and the pendulum angular velocity are considered in the sliding mode surface [20].

The sliding mode surface is defined as follows:

$$s = \omega_r - \omega_{rd} - \rho(\beta - \beta_d) \tag{21}$$

The exponential convergence law is chosen:

$$\dot{s} = -\varepsilon \mathrm{sgn}(s) - ks \quad \varepsilon > 0, k > 0 \tag{22}$$

where k and ε are convergence law parameters greater than 0.

In order to solve the problems of vibration caused by the controller parameter ingestion and the frequent switching of the sliding mode surface due to the change of vehicle driving conditions, the hyperbolic tangent function $\tanh(s)$ is used instead of the $\mathrm{sgn}(s)$ function, which reduces the frequent vibration of the traditional sliding mode control.

Derivation of Equation (21) for the sliding mode surface yields the following:

$$\dot{s} = \dot{\omega}_r - \dot{\omega}_r - \rho(\dot{\beta} - \dot{\beta}_d) \tag{23}$$

Substituting Equation (1) into the joint solution of Equation (23) yields the additional transverse moment affecting the vehicle’s transverse angular velocity, as follows:

$$\Delta M_{wr} = I(-\varepsilon \tanh - ks + \dot{\omega}_{rd}) - (ak_f - bk_r)\beta - \frac{a^2k_f + b^2k_r}{v} wr + ak_f\delta_f + I\rho\dot{\beta} \tag{24}$$

In the active transverse moment stability control, when the vehicle’s center of mass lateral deflection angle increases, at this time, the DYC system should increase the controller weights of the center of mass lateral deflection angle to ensure the vehicle’s stable driving and improve the vehicle’s attitude and path tracking ability. The phase diagram instability degree ρ affected by vehicle speed, road surface adhesion coefficient, and vehicle speed can respond well to the state of the vehicle and can assign the weights of the center of mass lateral eccentricity in the DYC system.

4.3. Lower Torque Distribution

Based on the target transverse moment calculated from the upper level, the ΔM is assigned to the vehicle hub motor through torque to enhance the stability of the vehicle. The lateral and longitudinal tire forces are limited by the attachment ellipse, and with the optimization objective of minimizing the utilization of tires [21], the optimal torque distribution is used. The tire utilization is as follows:

$$J = \sum_{i=1}^{4} \frac{{F_{xi}}^2}{(uF_{zi})^2} \tag{25}$$

To optimize the four-wheel longitudinal forces while ensuring the tracking of the vehicle speed, the constraints satisfy the following equations:

$$\begin{cases} F_x = F_{x1} + F_{x2} + F_{x3} + F_{x4} \\ \Delta M = \frac{B_f}{2}(F_{x2} - F_{x1}) + \frac{B_r}{2}(F_{x4} - F_{x3}) \end{cases} \tag{26}$$

The above optimization problem with constraints is organized as follows, using the standard form of dynamic optimization:

$$\begin{array}{l} \min J = \frac{1}{2}(\mathrm{u} - u_d)^T H(u - u_d) \\ s.t. Bu = V; u_{\min} \leq u \leq u_{\max} \end{array} \tag{27}$$

The value of torque enforcement after optimal distribution of tires on the vehicle is as follows:

$$T_{xi} = F_{xi} B_f,\ i = 1,2,3,4 \tag{28}$$

The total driving torque of the tracked vehicle calculated by the upper driver model is distributed equally among the four wheels, and the target yaw torque is distributed by the differential drive of the left and right wheels.

5. Road Simulation Analysis

In order to verify the effectiveness of the vehicle path tracking and stability cooperative control system, this paper adopts Matlab/Simulink and Carsim for joint simulation and selects the C-class vehicle as the simulation model. The tracking accuracy of the vehicle-designed path tracking controller is verified in the double-shift line condition at different speeds. Under the extreme working conditions of high-speed continuous lane changing and low-speed U-shape lane changing, the path tracking and stability cooperative control system designed in this paper is verified to ensure the vehicle path tracking effect and improve the stability of the vehicle at the same time.

5.1. Simulation Analysis of Double-Shifted Path Tracking

The common double shift roadway change condition is used. The reference heading angles and roadway turns for the double shift roadway are calculated as follows:

$$\theta_r = \arctan\{y_r'[x_r(t)]\}; k_r = \frac{y_r''[x_r(t)]}{\left(1 + y_r'[x_r(t)]^2\right)^{3/2}} \tag{29}$$

where k_r is the reference path curvature and θ_r is the reference heading angle.

The path tracking simulation verification of the path tracking front wheel steering (AFS) controller weight matrix parameters before optimization and after optimization of the genetic algorithm is performed for the dual-shift line under the dual-shift line condition with a vehicle speed of 60 km/h, respectively, and the simulation results are shown in Figures 9–12.

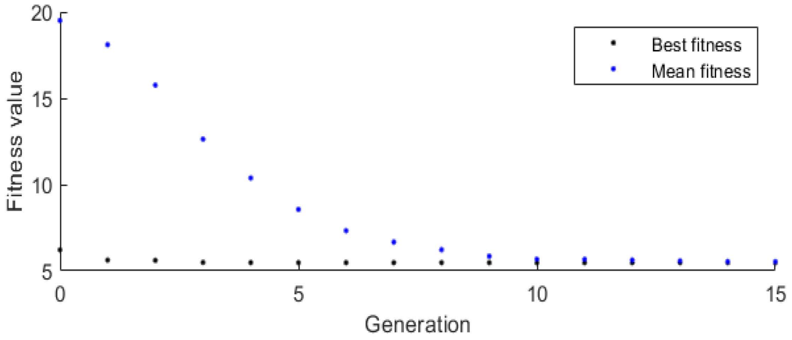

Figure 9. Genetic algorithm fitness values.

Figure 9 shows an image of the fitness function calculated by the genetic algorithm. The fitness function of the genetic algorithm gradually decreases from 18.93 to 3.77, and the optimization is terminated after the genetic generations to 15, when the fitness value is minimum and the initial parameters of the designed controller, Q and R matrices are

Q = diag [1, 1, 1, 1] and R = 80. After genetic optimization, the weights matrices are Q = diag [19.21, 1.22, 55.50, 1.01] and R = 99.40.

Figure 10 illustrates the vehicles' path comparison, highlighting the superior path tracking accuracy of the GA_LQR-controlled vehicle over the initial LQR-controlled vehicle, attributed to the optimization of controller parameters. The enhanced tracking effect of GA_LQR is evident at both 95 m and 145 m in the figure. Figure 11 presents a comparison of the vehicles' lateral errors, revealing a greater reduction in lateral error for the GA_LQR-controlled vehicle compared to the LQR-controlled vehicle. The maximum lateral error decreases from 0.0784 m to 0.0105 m, marking an 86.6% decrease, and the root mean square lateral error is reduced by 91.2%. The optimized GA_LQR controller enhances the vehicle's path tracking accuracy. Figure 12 compares the heading errors of the vehicles, indicating a reduction in the heading error for the GA_LQR-controlled vehicle compared to the LQR-controlled vehicle. The maximum heading error decreases from 0.0635 rad to 0.048 rad, representing a 17.7% reduction, and the root mean square heading error is reduced by 18.4%. The optimized GA_LQR vehicle exhibits a smaller heading error, signifying an improved heading angle tracking ability. The evaluation indexes for double-shifted line path tracking are presented in Table 2.

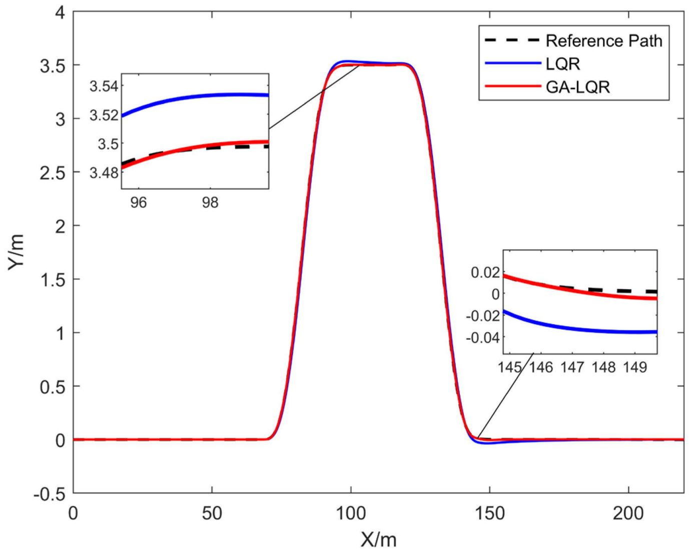

Figure 10. Vehicle path tracking map.

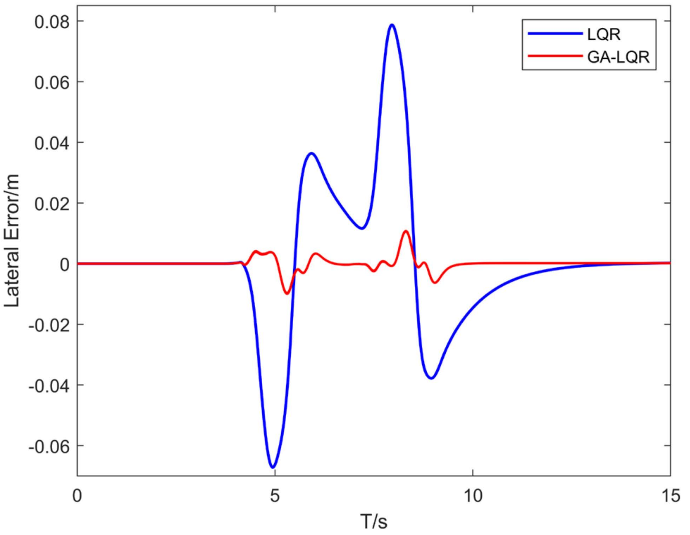

Figure 11. Vehicle lateral error map.

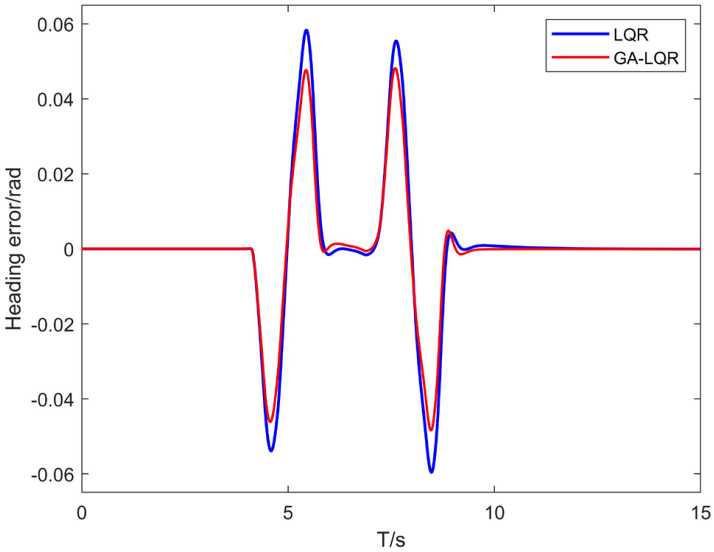

Figure 12. Vehicle heading error map.

Table 2. Evaluation indicators for double-shift path tracking.

Evaluation Index	LQR	GA_LQR	Optimal Results
∣ed∣ maximum value	0.0784	0.0105	86.6%
ed root mean square	0.0238	0.0021	91.2%
∣ephi∣ maximum value	0.0583	0.0480	17.7%
ephi root mean square	0.0179	0.0146	18.4%

To assess the robustness of the PID speed tracking controller and GA_LQR path tracking controller proposed in this study, vehicle tests are conducted at varying speeds, namely 36 km/h, 72 km/h, and 108 km/h. The effectiveness of both speed and path tracking is evaluated under double-shift line conditions, with the results presented in Figures 13 and 14.

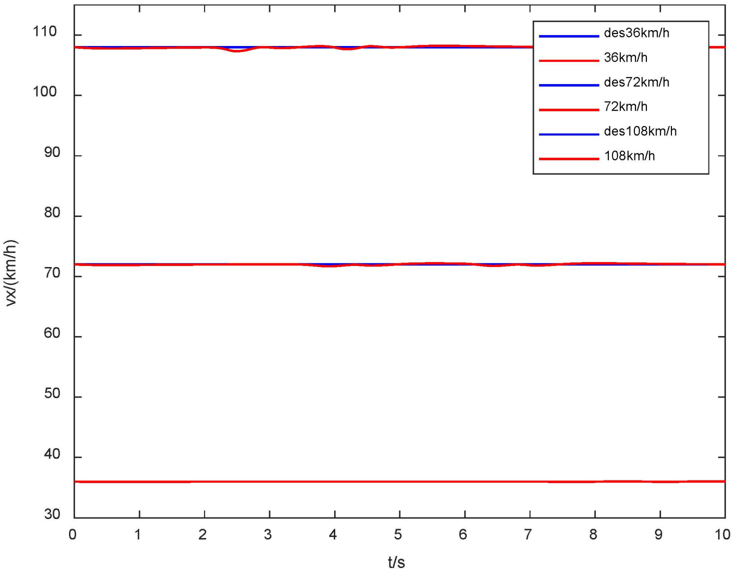

Figure 13. Longitudinal Speed Tracking.

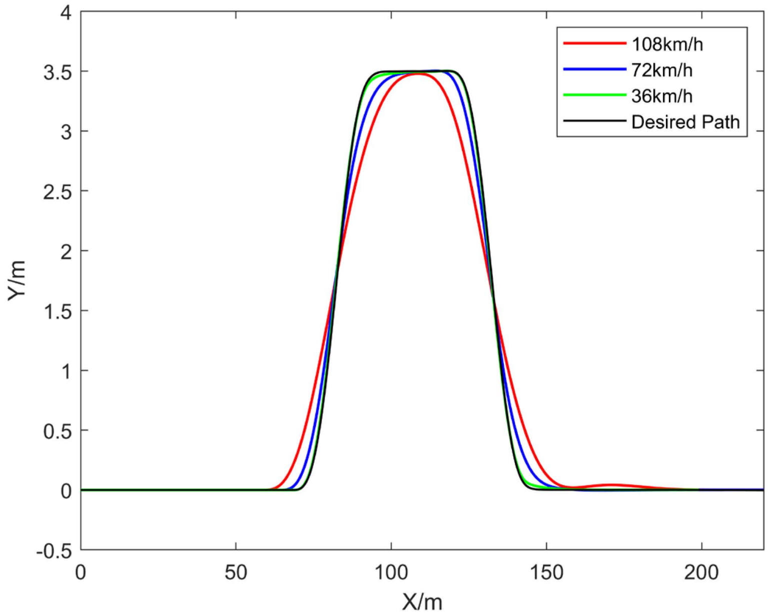

Figure 14. Path tracking at different speeds.

From Figure 13, it can be seen that the PID speed tracking controller designed for the longitudinal direction of the vehicle is able to track the upper desired speed better whether it is at low, medium, or high speeds and the maximum speed error is not more than 1 km/h. The longitudinal speed controller has a better speed tracking ability at different speeds. The designed GA_LQR path tracking controller has better tracking ability at low speeds. At a medium speed of 72 km/h and a high speed of 108 km/h, due to the fast speed of the vehicle changing lanes, in order to ensure that the vehicle can be well tracked on the path, it is necessary to increase the pre-aiming control on the basis of the path tracking control of the vehicle. At the speeds of 72 km/h and 108 km/h, this paper adopts the pre-aiming time of 0.2 s and 0.4 s, respectively, to ensure that the vehicle can make advance judgment on the path change and control the front wheel angle. Figure 14, depicting the vehicle path diagram, demonstrates that, after incorporating GA_LQR control with pre-scanning, the vehicle effectively tracks the desired path across low, medium, and high speeds. Consequently, the vehicle path tracking controller and speed controller developed in this paper exhibit robust performance across different speeds.

5.2. Simulation Analysis of Continuous Lane Change Path Tracking

In the simulation test where the vehicle is subjected to continuous lane changing, the road equations for continuous lane changing are as follows:

$$Y(X) = \frac{c}{2\pi}\left\{\pi + \frac{2\pi}{d}(X - \frac{d}{2}) + \sin\left[\frac{2\pi}{d}(X - \frac{d}{2})\right]\right\} \tag{30}$$

where c is the value of 50 m for the transverse displacement of the changeover and d is the value of 3.5 m for the longitudinal displacement of the changeover.

Under the conditions of a vehicle speed of 120 km/h, a pavement adhesion coefficient of 0.7, and a pre-sighting time of 0.3s, a simulation is conducted to assess continuous lane-changing scenarios. The considered control strategies include AFS control, AFS+DYC synergistic control, and the path tracking and stability controller (Controller 1) adopted from reference [22], each executed independently. The Controller 1 system utilizes the conventional path tracking method involving single-point pre-scanning and considers the center of mass side deflection angle, along with the active transverse moment composition of the transverse angular velocity sliding mode surface. The results of these control simulations are presented in Figure 15.

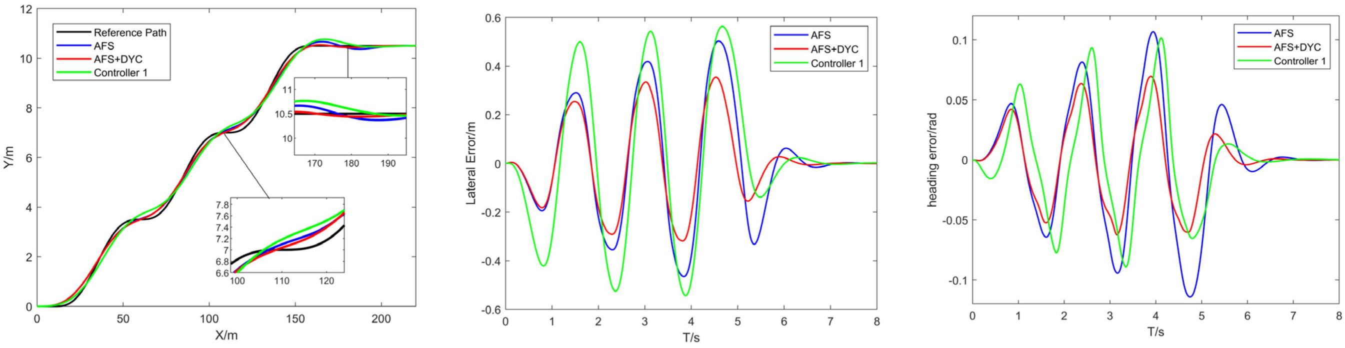

(a)Vehicle travel path (b)Vehicle lateral error (c)Vehicle heading error

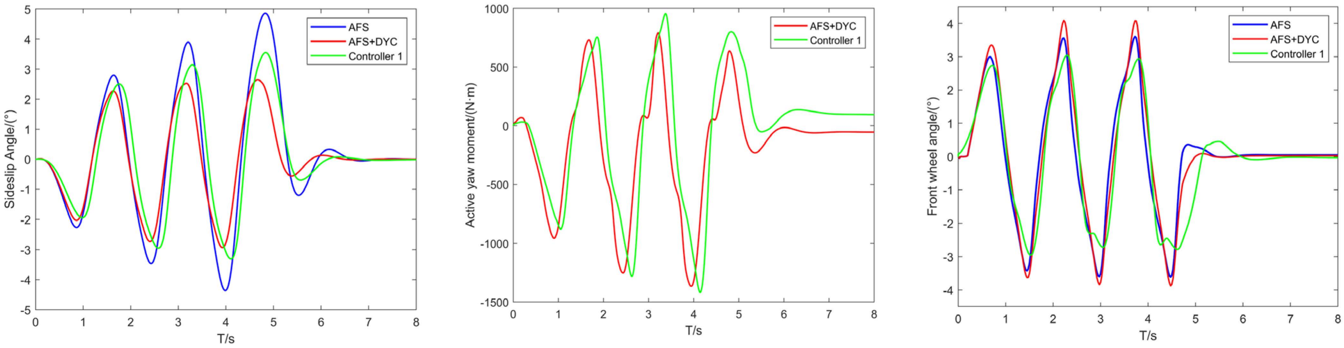

(d)Vehicle Sideslip angle (e)Active yaw moment (f)Front wheel angle

Figure 15. Simulation results of continuous lane changing conditions.

Figure 15a,b depict the travel paths and lateral errors of the vehicle under high-speed continuous lane changing conditions. All three controllers successfully track the desired paths. However, the AFS control and Controller 1 exhibit larger path fluctuations at 170 m and 110 m, whereas the designed AFS+DYC controller demonstrates the smallest path offset, closely aligning with the desired paths. The peak lateral error of Controller 1 reaches a maximum of 0.56 m, and the vehicle's path tracking deteriorates under continuous lane changing conditions with faster speed, due to the reliance on single-point pre-scanning control. The path tracking controller optimized with parameters (AFS) designed in this paper exhibits a slight improvement in tracking effect compared to Controller 1, with the peak lateral error of the vehicle being 0.50 m. The peak lateral error of AFS+DYC control is 0.35, representing a 37.5% reduction compared to AFS control. This results in the best path tracking effect, and the introduction of direct swinging torque control on the basis of AFS control enhances the vehicle's lateral path tracking during high-speed continuous lane changing. In Figure 15c, the heading error of the vehicle is depicted, and the AFS-controlled vehicle exhibits the largest peak heading error, reaching 0.11 rad. Compared with AFS path tracking control, Controller 1 incorporates active transverse moment control based on path tracking control, resulting in a slight reduction in peak heading deviation to 0.10 rad, a reduction of 9%. The AFS+DYC-controlled vehicle, influenced by the active transverse moment and adjusting the control weight for vehicle stability based on the center of mass side deviation angle, achieves a reduced peak heading error of 0.06 rad, which is 40% lower than AFS control. The AFS+DYC controller enhances the vehicle's ability to track the heading angle under high-speed lane changing conditions. Figure 15d illustrates the vehicle's sideslip angle, with the AFS-controlled vehicle reaching a peak vehicle's sideslip angle of 4.85° attributed to high speed and continuous lane changing. At this point, the vehicle approaches an unstable state, requiring intervention for stability control. With the intervention of the direct swing moment, Controller 1 reduces the peak vehicle's sideslip angle deviation of the vehicle to 3.55°, representing a 9% reduction. The AFS+DYC control, as designed in this paper, achieves further suppression of the vehicle's center of mass lateral deflection through coordinated weight allocation of the

DYC controller. The peak of the vehicle's sideslip angle is minimized to 2.63°, reflecting a 45.5% reduction compared to the peak value of the AFS control, resulting in enhanced vehicle driving stability. Figure 15e illustrates the direct transverse moment computed by the vehicle's DYC system, which serves to enhance vehicle stability at high speeds, while ensuring effective path tracking. In comparison to the fixed parameter calculation of the active transverse moment by Controller 1, the AFS+DYC controller computes a direct transverse moment, taking into account the instability of the vehicle, and achieves a balanced coordination of path tracking and stability. This results in a further improvement in vehicle stability and path tracking capability. The active traverse moment is ultimately output through the differential distribution of torque among the four wheels. Figure 15f illustrates the front wheel steering angle of the vehicle tracking the desired path. The front wheel steering is increased by the AFS+DYC control, but the front wheel steering angles remain within the stable range, ensuring the vehicle can track the desired path. The stability evaluation indexes for continuous lane changing are shown in Table 3 below.

Table 3. Continuous lane changing simulation evaluation index data.

Evaluation Index	AFS	Controller 1	Compare AFS Results	AFS+DYC	Compare AFS Results
Lateral error ∣ed∣	0.50	0.56	−0.12%	0.35	37.5%
Heading error ∣ephi∣	0.11	0.10	9%	0.06	40%
Sideslip angle $\lvert\beta\rvert$	4.85	3.55	26.8%	2.63	45.5%

5.3. Low-Speed Turnaround Path Tracking Simulation Analysis

In order to further verify the controller designed in this paper, the low-speed turnaround condition is selected, and the vehicle is driven at a speed of 20 km/h on the ice and snow road, with the road adhesion coefficient μ = 0.3 and the simulation results are shown in Figure 16.

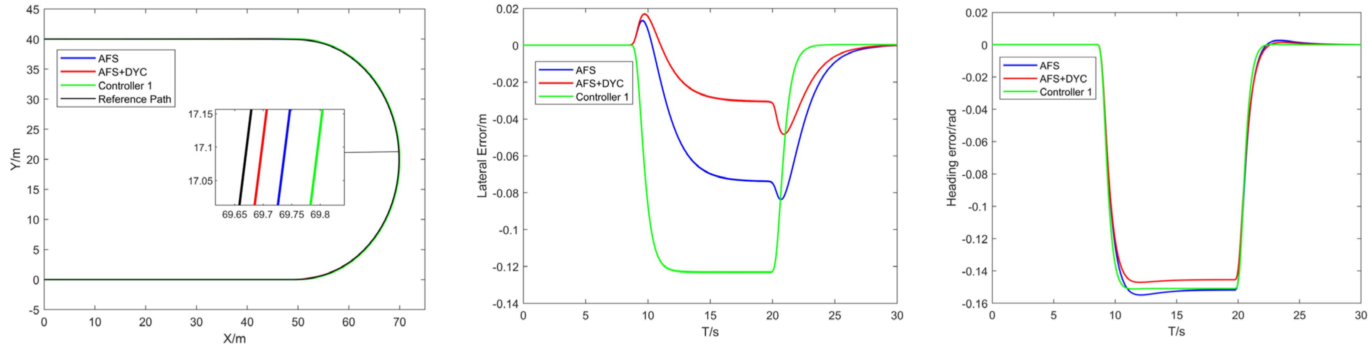

(a)Vehicle travel path (b)Vehicle lateral error (c)Vehicle heading error

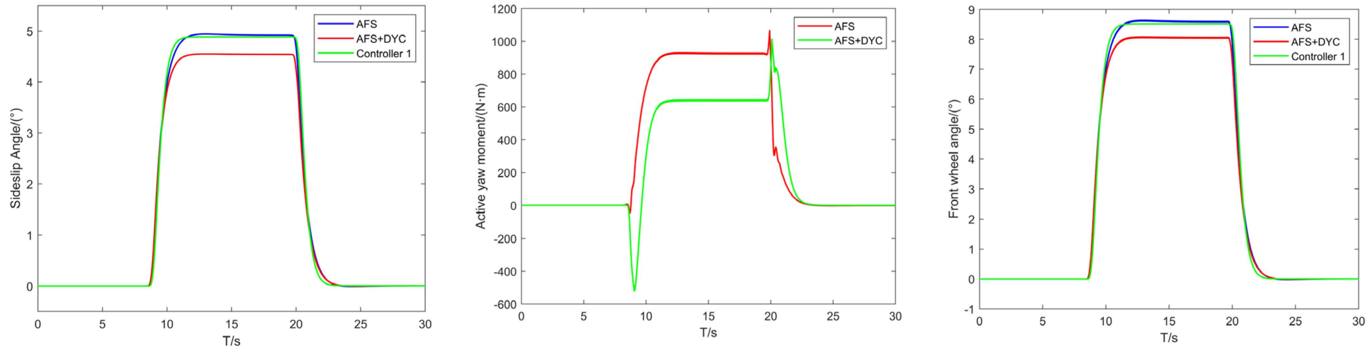

(d)Vehicle Sideslip angle (e)Active yaw moment (f)Front wheel angle

Figure 16. Simulation results of low-speed turning conditions.

Figure 16a,b illustrate the vehicle's traveling paths and lateral errors during the turnaround on the wet road. All three controllers effectively track the upper desired turnaround path. It is evident that the path tracking accuracy of the AFS+DYC cooperative control surpasses that of both Controller 1 and the AFS-controlled vehicle. Controller 1 and AFS+DYC exhibit peak lateral errors of 0.083 m and 0.046 m, respectively, representing reductions of 51.8% and 62.6% compared to the AFS control. The AFS+DYC control demonstrates superior path tracking and closely aligns with the desired path, enhancing vehicle tracking on icy, snowy, and slippery road surfaces.

In Figure 16c, the vehicle's heading error is presented, with the AFS vehicle reaching a peak deviation of 0.155 rad. Controller 1 and AFS+DYC exhibit peak deviations of 0.151 rad and 0.145 rad, respectively, indicating marginal reductions of 4% and 6.5% compared to AFS. The direct traverse moment control enhances the vehicle's heading angle tracking ability. The incorporation of stability control, based on AFS path tracking, has effectively mitigated both lateral and heading errors in the vehicle.

Figure 16d displays the vehicle sideslip angle, with the peak angle reaching 4.94° for the AFS-controlled vehicle. During this period, the vehicle approaches an unstable state, and its body attitude becomes precarious, necessitating additional controls for stability. Controller 1 and the AFS+DYC-controlled vehicle experience additional sway moments, resulting in a reduction in the peak center of mass lateral deflection angle to 4.88° and 4.54°, respectively. This reduction represents a 7.5% and 8.0% improvement compared to the AFS-controlled vehicle. The AFS+DYC-controlled vehicle provides the best suppression of vehicle sideslip angle control, which improves the stability and path tracking ability of the vehicle when traveling in a U-turn on a low adhesion road. In Figure 16e, the direct traversing moment demanded by the vehicle DYC system is illustrated. Subsequently, the additional traversing moment is utilized to implement stability control through optimal torque distribution among the four wheels via motor output torque. Figure 16f displays the front wheel turning angle as the vehicle tracks the desired path, with AFS+DYC requiring a minimal turning angle, contributing to improved operational stability. The stability evaluation indexes under U-turn conditions are presented in Table 4 below.

Table 4. U-shaped path simulation evaluation index data.

Evaluation Index	AFS	Controller 1	Compare AFS Results	AFS+DYC	Compare AFS Results
Lateral error ∣ed∣	0.123	0.083	51.8%	0.046	62.6%
Heading error ∣ephi∣	0.155	0.151	4%	0.145	6.5%
Sideslip angle $\|\beta\|$	4.94	4.88	7.5%	4.54	8.0%

6. Conclusions

To enhance intelligent vehicle path tracking while ensuring stability, a cooperative controller for both vehicle path tracking and stability is proposed. For vehicle path tracking, a vehicle error dynamics model is established, and a laterally designed path tracking LQR controller with pre-scanning is employed. To address uncertainties in controller parameters, a genetic algorithm is utilized to design a fitness function and optimize the weight matrix. This approach enhances the vehicle's path tracking ability and ensures accurate path tracking, especially on conventional roads.

To enhance vehicle stability based on vehicle path tracking, the process begins by fitting the vehicle tire side deflection force. Subsequently, the phase plane of the vehicle center of mass side deflection angle is plotted, and the double straight line method is employed to delineate the stability region. A three-dimensional boundary map of the vehicle stability domain is then generated, and the degree of vehicle instability is calculated under various working conditions. And based on the hyperbolic tangent function of the sliding mode control design of the active transverse moment, through the vehicle instability degree of the active transverse moment of the sliding mode surface of the center of mass side deflection, the control weights are adjusted to improve the driving stability of the vehicle. In scenarios involving high-speed continuous lane changes and low-speed turns on low-adhesion roads, the proposed approach ensures effective vehicle path tracking while concurrently enhancing vehicle stability.

Author Contributions: Conceptualization, Z.D. and Y.Z.; methodology, Y.Z.; software, Y.Z.; validation, Z.D., S.Z. and Y.Z.; formal analysis, Y.Z.; investigation, S.Z.; resources, S.Z.; data curation, Y.Z.; writing—original draft preparation, Y.Z.; writing—review and editing, Z.D.; visualization, Z.D.; supervision, Z.D.; project administration, S.Z.; funding acquisition, S.Z. All authors have read and agreed to the published version of the manuscript.

Funding: This research was funded by National Natural Science Foundation of China (52072054); The Science and Technology Research Program of Chongqing Municipal Education Commission (KJQN202100728); Graduate Scientific Research and Innovation Foundation of Chongqing Jiaotong University (2022S0042); The special support for Chongqing postdoctoral research project (2022COBSHTB1004).

Data Availability Statement: The original contributions presented in the study are included in the article, further inquiries can be directed to the corresponding author.

Conflicts of Interest: The authors declare no conflicts of interest.

References

1. Li, K.Q.; Dai, Y.F.; Li, S.B.; Bian, M.Y. Development Status and Trends of Intelligent Connected Vehicle (ICV) Technology. *J. Automot. Saf. Energy Sav.* **2017**, *8*, 1–14.
2. Dai, D.; Chen, Z.; Bao, P.; Wang, J. A Review of 3D object detection for autonomous driving of electric vehicles. *World Electr. Veh. J.* **2021**, *12*, 139. [CrossRef]
3. He, S.; Fan, X.; Wang, Q.; Chen, X.; Zhu, S. Review on Torque Distribution Scheme of Four-Wheel In-Wheel Motor Electric Vehicle. *Machines* **2022**, *10*, 619. [CrossRef]
4. Karahan, O.; Ataslar-Ayyildiz, B. Optimal design of fuzzy PID controller with cs algorithm for trajectory tracking control. *Adv. Intell. Syst. Comput.* **2019**, *858*, 174–188.
5. Zhang, Y.; Xia, Y.; Cheng, H.; Lv, L. Research on Path Tracking Lateral Control of Intelligent Vehicles. *J. Chongqing Univ. Technol. (Nat. Sci. Ed.)* **2021**, *35*, 53–61.
6. Awad, N.; Lasheen, A.; Elnaggar, M.; Kamel, A. Model predictive control with fuzzy logic switching for path tracking of autonomous vehicles. *ISA Trans.* **2022**, *129*, 193–205. [CrossRef]
7. Luan, Z.; Zhang, J.; Zhao, W.; Wang, C. Trajectory Tracking Control of Autonomous Vehicle with Random Network Delay. *IEEE Trans. Veh. Technol.* **2020**, *69*, 8140–8150. [CrossRef]
8. Meng, Y.; Gan, X.; Wang, Y.; Gu, Q. LQR-GA controller for articulated dump truck path tracking system. *J. Shanghai Jiaotong Univ. (Sci.)* **2019**, *24*, 78–85. [CrossRef]
9. Zhao, C.; Zhang, C.; Guo, F.; Shao, Y. Research on Path Following Control Method of Agricultural Machinery Autonomous Navigation through LQR-Feed Forward Control. In Proceedings of the 2021 IEEE International Conference on Data Science and Computer Application (ICDSCA), Dalian, China, 29–31 October 2021; pp. 228–323.
10. Gao, L.; Tang, F.; Guo, P.; He, J. Research on Improved LQR Method for Autonomous Driving Lateral Motion Control. *Mach. Sci. Technol.* **2021**, *40*, 435–441.
11. Zhang, L.; Wu, G. *Combination of front Steering and Differential Braking Control for the Path Tracking of Autonomous Vehicle*; SAE Technical Paper 2016-01-1627; SAE International: Warrendale, PA, USA, 2016.
12. Nie, Y.; Zhang, M.; Zhang, X. Trajectory Tracking Control of Intelligent Electric Vehicles Based on the Adaptive Spiral Sliding Mode. *Appl. Sci.* **2021**, *11*, 11739. [CrossRef]
13. Chen, T.; Chen, L.; Xu, X.; Cai, F.; Jiang, H. Path Tracking and Stability Coordinated Control of Distributed Driverless Vehicles. *Automot. Eng.* **2019**, *41*.
14. Zhao, S.; Hu, H.; Jing, D. Stability Control of Distributed Drive Electric Vehicle Based on AFS/DYC Coordinated Control. *J. Huaqiao Univ. (Nat. Sci. Ed.)* **2021**, *42*, 571–579.
15. Liang, Y.; Li, Y.; Yu, Y.; Zheng, L. Integrated lateral control for 4WID/4WIS vehicle in high-speed condition considering the magnitude of steering. *Veh. Syst. Dyn.* **2020**, *58*, 1711–1735. [CrossRef]
16. Rajamani, R. *Vehicle Dynamics and Control*; Springer Science Business Media: New York, NY, USA, 2011.
17. Marada, T.; Matousek, R.; Zuth, D. Design of linear quadratic regulator (LQR) based on genetic algorithm for inverted pendulum. *Mendel* **2017**, *23*, 149–156. [CrossRef]
18. Guo, L.; Wei, L.; Ge, P.; Qin, Z. Lane Keeping Controller based on LQR Optimized by Genetic Algorithm. In Proceedings of the 2022 6th CAA International Conference on Vehicular Control and Intelligence (CVCI), Nanjing, China, 28–30 October 2022; pp. 1–6.

19. Yang, K.; Dong, D.; Ma, C.; Tian, Z.; Chang, Y.; Wang, G. Stability Control for Electric Vehicles with Four In-Wheel-Motors Based on Sideslip Angle. *World Electr. Veh. J.* **2021**, *12*, 42. [CrossRef]
20. Zhang, C.; Wang, Z.; Cheng, J.; Liu, J. 4WIS-4WID vehicle yaw stability AFS+ARS+DYC sliding mode control. *Automot. Eng.* **2014**, *36*. [CrossRef]
21. Lu, M.; Xu, Z. Integrated Handling and Stability Control with AFS and DYC for 4WID–EVs via Dual Sliding Mode Control. *Autom. Control. Comput. Sci.* **2021**, *55*, 243–252. [CrossRef]
22. Xiang, J.; Zhou, K.; Fu, Y.; Xu, Y.; Peng, X. Research on 4WD/4WS unmanned vehicle path tracking control strategy considering stability. *Comput. Eng. Appl.* **2023**, 1–11.